Appl. Phys. B 76, 859–867 (2003)
DOI: 10.1007/s00340-003-1231-6

Applied Physics B
Lasers and Optics

D. AUMILER✉
T. BAN
R. BEUC
G. PICHLER

Simultaneous determination of the temperature and density of rubidium vapor

Institute of Physics, Bijenička 46, P.O. Box 304, 10001 Zagreb, Croatia

Received: 15 February 2003/Revised version: 17 May 2003
Published online: 16 July 2003 •

ABSTRACT We propose a new method for the simultaneous determination of the temperature and atom number density in rubidium vapor. The method is based on the comparison of theoretical simulations of the self-broadened absorption profiles of rubidium resonance lines with the measured profiles. Absorption measurements performed in rubidium vapor indicate that in the spectral region around resonance lines (760–835 nm), excellent agreement between theoretical and experimental absorption profiles can be achieved. In the temperature interval 500–700 K, the simultaneous determination of the atom number density and temperature of rubidium vapor is possible. We have applied the present method to nearly homogeneous and inhomogeneous rubidium vapors generated in a sapphire cell.

PACS 31.15.Gy; 32.30.Jc; 32.70.-n

1 Introduction

The measurement of particle density and temperature is one of the most important elements of an experiment, having far reaching effects on any subsequently measured physical quantities [1, 2].

In the case of a pure metal vapor, the standard procedure for atom number density determination is based on the vapor pressure curve [3, 4]. However, in order to determine the atom number density accurately, one has to know the exact temperature of the system. The uncertainty in the measured temperature of the system, together with the uncertainty of the relevant vapor pressure curve, limits the accuracy of atom number density determination. To avoid this uncertainty, several spectroscopic methods that do not require an accurate knowledge of the vapor temperature have been developed.

Spectroscopic methods for the determination of the atom number density basically can be divided into two groups. In the first group the atom number density is determined by measuring the integral of the spectral line absorption coefficient. This method is usually applicable at low particle densities, at which the optically thin spectral lines can be evaluated by using known oscillator strengths. However, by using the usual curve of the growth technique [5, 6] it is also possible to use the optically thick lines for density determination. For accurate use of this method, the ratio of the Lorentzian and Doppler half-widths must be known. The main factor limiting the accurate determination of the atom number density with this method is the uncertainties in the values of these half-widths at high vapor pressures. In the present case, only the higher members of the Rb principal series lines could be candidates for density determination.

The second group of spectroscopic methods for atom number density determination is based on comparisons between the experimental and theoretical absorption coefficient profiles. The self and foreign-gas broadening of first rubidium resonance lines has been widely investigated experimentally and theoretically (see e.g. [7, 8]). The use of just one extended quasi-static wing of the first resonance lines of alkali vapor for atom density determination has been presented in several publications [9, 10].

However, all these established spectroscopic methods fail to accurately determine high atomic densities at elevated temperatures. Therefore, we believe that a good knowledge of long- and short-range interaction potential curves, together with a good knowledge of the relevant transition dipole moment functions, which are presently available, offers an excellent opportunity for constructing reliable spectral profiles of resonance lines in the Franck–Condon region (extended quasi-static line wings). These spectral profiles can be easily used for a two-parameter fit of the experimental data.

In the present paper we suggest a new method for the simultaneous determination of the atom number density and temperature of rubidium vapor. The method relies on our theoretical calculations of the full profiles of first rubidium resonance lines in the wavelength range 760–835 nm, and in the temperature interval 500–700 K. For a comparison with experimentally obtained absorption profiles, theoretical simulations of the absorption coefficient profiles were performed. We applied this method for the determination of the effective atom number density and temperature of a nearly homogeneous rubidium vapor generated in a sapphire cell. The assumption of homogeneity is of considerable importance, although in many situations it is far from a reality. Therefore it is of some interest to study the real experimental situation, in which we deliberately impose some inhomogeneous structure, and to compare the results of the simulations with experiment. The physical

✉ Fax: +385-1/4698-889, E-mail: aumiler@ifs.hr

conditions of the inhomogeneous rubidium vapor inside the cell were characterized using a simple temperature diffusion model. Even under such conditions, we show that important information on an average (effective) temperature and atom density may be obtained.

This method may be applied to other alkali metals. However, the corresponding accurate calculations of the absorption coefficient profiles and a discussion of constraints would be necessary in each particular case.

2 Experiment

In order to test our method, simple absorption measurements in a linear all-sapphire cell (ASC) [11–13] were performed. The cylindrical all-sapphire cell used in the experiment was 120 mm long (without windows) with a 10.4-mm inner diameter and 13.5-mm outer diameter. It was filled with pure rubidium metal and evacuated. The cell was placed in an oven, which consisted of two identical parts. Each part consisted of a 100-mm-long quartz tube, with a nichrome wire uniformly wound around the tube. Firebricks thermally isolated the quartz tubes. The temperatures were measured by three thermocouples placed at the central point and two side points of the cell, in contact with the outer wall of the cell. The temperature T_o between the two parts of the oven was about 15–20 K lower than the temperatures T_1 of the side parts. This ensured clean windows of the cell during the measurements.

For an even more inhomogeneous rubidium vapor density distribution, a new heater was inserted between the two identical side parts of the oven. It was made from a 5-mm-thick aluminum ring that was connected to an aluminum arm heated at the end by a Thermocoax heater [14]. For the sake of clarity a schematic of the oven and sapphire cell is shown in Fig. 1. The side parts of the cell were always kept at higher temperatures than the central part, with the temperature difference being up to 150 K.

In such an arrangement, the rubidium vapor pressure inside the cell is determined by the lowest temperature point within the central part of the cell. The rubidium atom concentration in the cell follows the equation of state for a perfect gas [15], and is not uniform across the whole volume of the cell.

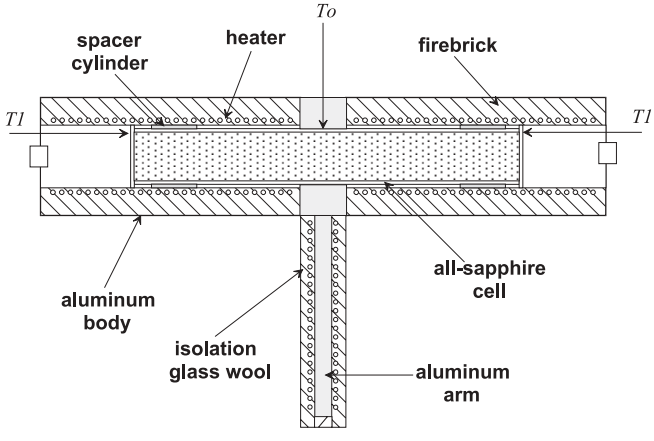

FIGURE 1 Schematic of the heater arrangement in the oven used for the generation of an inhomogeneous rubidium vapor in the sapphire cell

Continuous light from an infrared LED irradiated the rubidium vapor. The direction of propagation of the continuous light was parallel to the optical axis of the sapphire window, thus avoiding birefringent effects. After passing through the absorption cell the light was collected by a cylindrical lens and focused onto the entrance slit of a 1.5-m Jobin Yvon THR scanning monochromator. The monochromator was equipped with a 1200-grooves/mm holographic grating, resulting in resolution of 0.04 nm at a slit width of 30 μm. The light at the exit slit of the monochromator was detected photoelectrically, using a Hamamatsu SR936 photomultiplier tube. The signal was amplified by a Stanford Research Systems SR510 lock-in amplifier (connected to a SR560 mechanical light chopper) and stored on a laboratory PC.

Absorption measurements of the rubidium vapor were performed in the spectral region that includes the Rb $5s_{1/2} \rightarrow 5p_{1/2,3/2}$ first resonance lines, from approximately 760 to 835 nm. The absorption coefficient $k(\lambda)$ of the rubidium vapor at a temperature T can be obtained experimentally from the Beer-Lambert law:

$$k(\lambda) = \frac{1}{L} \ln \frac{I_0(\lambda)}{I_L(\lambda)} , \tag{1}$$

where L is the length of the absorbing vapor column, $I_L(\lambda)$ the intensity of the light transmitted through rubidium vapor at temperature T, and $I_0(\lambda)$ is the intensity of the light transmitted through the sapphire cell at room temperature. Prior to each set of measurements (at different temperatures T) $I_0(\lambda)$ was measured at room temperature. After all experimental runs and cell cooling, $I_0(\lambda)$ was measured again. We established that the shape of the $I_0(\lambda)$ function remained unchanged during the measurements. This is a result of stable infrared LED emission, which is an advantage over conventional halogen-lamp white-light sources. However, the absolute value of $I_0(\lambda)$ increased with increasing temperature. This problem was related to the coating of the cell windows during the cooling process, which resulted in a reduced absolute value of $I_0(\lambda)$. These thin alkali layers on the sapphire windows acted like a gray filter. Therefore, during the absorption measurement the effective continuum intensity was $\alpha I_o(\lambda)$, where α is a temperature-dependent multiplicative factor with a value $\alpha > 1$. As a consequence, the measured absorption coefficient at each temperature had an additional constant background, which was typical for each set of measurements and increased with increasing temperature of the vapor. Taking this into account, we have modified (1) by

$$k_{\text{exp}}(\lambda) = \frac{1}{L} \ln \frac{I_0(\lambda)}{I_L(\lambda)} + \frac{1}{L} \ln \alpha . \tag{2}$$

By increasing the cell temperature the thickness of the thin films decreased. Under our experimental conditions of dense rubidium vapor, there was no convenient spectral window that could be used for the determination of the value of α. Nevertheless, this constant background could be estimated by using the procedure described in detail above.

3 Theory

In order to calculate the rubidium absorption coefficient in the measured wavelength region, we took into ac-

count the transitions connecting the Rb_2 ground states and all possible upper states having $Rb(5s_{1/2}) + Rb(5p_{1/2,3/2})$ molecular asymptotes. Hund's case (a) potential curves are built from ab initio potential curves [16] matched with long-range asymptotic calculations [17]. Based on these potentials we calculated a new set of Rb_2 potential curves with a spin–orbit coupling contribution (Hund's case (c)) and relevant molecular electronic transition dipole moment functions, using the semiempirical "atoms in molecules" scheme developed by Cohen and Schneider [18, 19].

Difference potentials between the upper gerade states with $Rb(5s_{1/2}) + Rb(5p_{1/2,3/2})$ molecular asymptotes and the ground $1(a)\ ^3\Sigma_u^+(0_u^-, 1_u)$ states are shown in Fig. 2a. In Fig. 2b we present difference potentials between the upper ungerade states with $Rb(5s_{1/2}) + Rb(5p_{1/2,3/2})$ molecular asymptotes and the ground $1(X)\ ^1\Sigma_g^+(0_g^+)$ state. The molecular states in Fig. 2a and b are labeled with the upper state designation.

The semiclassical quasi-static approximation described in detail in our previous paper [20] was used for the calculation of the absorption coefficient profiles. The linear absorption coefficient $k(\lambda, N, T)$ for the given wavelength λ, atom number density N, and vapor temperature T can be calculated by the following relation [21]:

$$k(\lambda, N, T) = N^2 \frac{4\pi^2 e^2 \hbar}{mc} \sum_{i,f} \sum_{c_{if}} \frac{R_{c_{if}}^2 f_{if}(R_{c_{if}})}{\left|\Delta'_{if}(R_{c_{if}})\right|} \times \exp(-(V_i(R_{c_{if}}) - V_i(\infty))/kT)\,. \quad (3)$$

The first summation in (3) is taken over all initial states i (electronic energy $V_i(R)$) and final molecular states f (electronic energy $V_f(R)$) for which optical transitions contribute to the absorption spectra in the region of the interest. For each transition there is a corresponding difference potential $\Delta_{if}(R) = V_f(R) - V_i(R)$, its first derivative $\Delta'_{if}(R)$, and the molecular oscillator strength $f_{if}(R)$. The latter is proportional to the statistical weight of the initial state and to the square of the matrix element of the electric dipole moment. The second summation is over all Condon points R_c that, for the given transition i–f, satisfy the classical Franck–Condon condition $\Delta_{if}(R_{c_{if}}) = \frac{hc}{\lambda}$ [22, 23].

The relation (3) is valid in the region of energy for which there are no extrema in the difference potential curve. However, from Fig. 2a it is evident that in the energy range of interest, several differential potentials possess extrema. The $(2)0_g^+$–1_u difference potential curve exhibits an extremum at intermediate internuclear distances, in the energy range very close to the center of the resonance D2 line. However, in the neighborhood of the line-center this transition gives a negligible contribution in comparison with all other transitions with the enormous absorption coefficient at the center of the 780-nm resonance line. In the case of the cesium dimer, the corresponding satellite band is located in between the two resonance lines [20]. The extrema belonging to the $(2)0_g^-$, $(3)1_g$, and $(1)2_g$ upper states are located approximately at 6.5 Bohr, where the short-range $1(a)\ ^3\Sigma_u^+$ ground state is very repulsive. Therefore, they do not contribute to the total absorption coefficient at these short-range internuclear distances, since the number of collisions at such high energies is negligible. The contributions to the total absorption coefficient from upper states of gerade symmetry come from the transitions at long-range internuclear distances, $R > 20$ Bohr. At these internuclear distances, the Rb_2 ground state $^3\Sigma_u^+$ potential is very shallow with a binding energy of less than $20\ cm^{-1}$ [16]. Consequently, the Boltzmann factor in (3) becomes approximately one. As a result, the absorption coefficients calculated for the optical transitions at long-range internuclear distances are temperature independent.

In the case of ungerade upper states (Fig. 2b), besides contributions at long-range internuclear distances, there is also a contribution to the total absorption coefficient that comes from transitions at short-range internuclear distances. In the energy range of interest the $(2)0_u^+$–$(1)0_g^+$ difference potential possesses two Condon points with the same energy but different internuclear distances (one at short-range, another one at long-range). The contribution to the absorption coefficient due to the interference of these Condon points is negligible because of their large separation. Therefore, each Condon point can be taken independently in the calculation of the total absorption coefficient at wavelengths λ close to resonance line. In the diabatic representation the $(2)0_u^+$ potential has

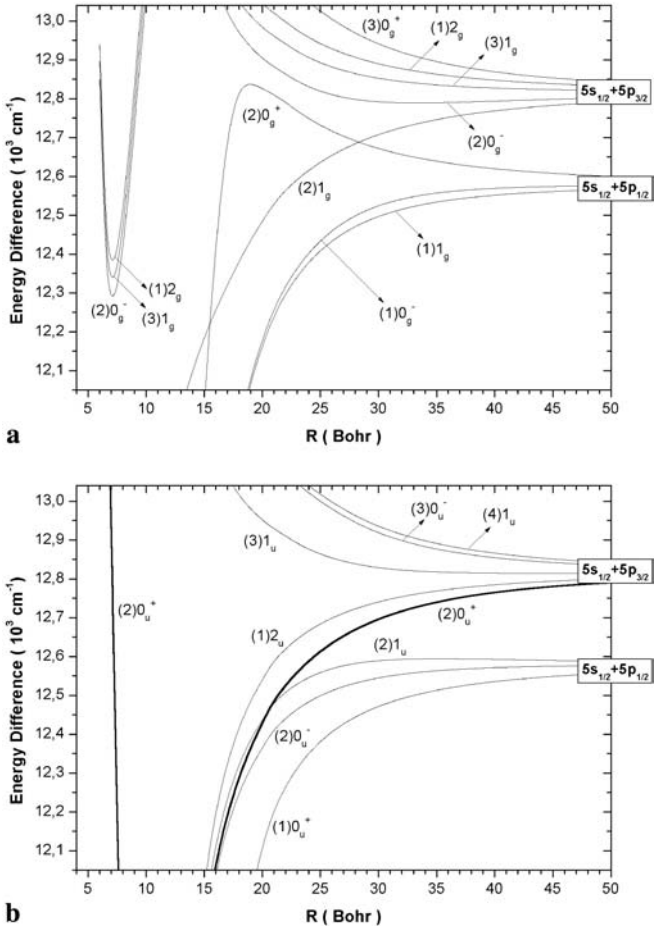

FIGURE 2 **a** Difference potentials between the gerade upper states with $Rb(5s_{1/2}) + Rb(5p_{1/2,3/2})$ molecular asymptotes and the ground $1(a)\ ^3\Sigma_u^+$ $(0_u^-, 1_u)$ states in the energy range of interest. **b** Difference potentials between the ungerade upper states with $Rb(5s_{1/2}) + Rb(5p_{1/2,3/2})$ molecular asymptotes and the ground $1(X)\ ^1\Sigma_g^+$ (0_g^+) state located in the energy range of interest

$^3\Pi_u$ symmetry at short internuclear distances. However, in the adiabatic representation, because of the avoided crossing with the $(1)0_u^+$ potential, the $(2)0_u^+$ potential exhibits $1(A)\ ^1\Sigma_u^+$ symmetry at short range [24]. The ground $(1)0_g^+$ potential has $1(X)\ ^1\Sigma_g^+$ symmetry at short internuclear distances.

Regarding this discussion it is evident that the total calculated absorption coefficient consists of two parts. The first one is temperature independent and comprises contributions from transitions at long-range internuclear distances (both gerade and ungerade upper states). The second part is temperature dependent and is related to $1(X)\ ^1\Sigma_g^+ \rightarrow 1(A)\ ^1\Sigma_u^+$ transitions at short-range internuclear distances. Thus, the total absorption coefficient for the optical transitions at wavelength λ can be calculated by modifying (3) in the following way:

$$k(\lambda, N, T) = N^2 \left[A(\lambda) + B(\lambda) \exp\left(C(\lambda)/T\right)\right] , \tag{4}$$

where the functions $A(\lambda)$, $B(\lambda)$, and $C(\lambda)$ are given by

$$A(\lambda) = \frac{4\pi^2 \mathrm{e}^2 \hbar}{mc} \sum_{i,f} \frac{R_{c_{if}}^2 f_{if}(R_{c_{if}})}{\left|\Delta'_{if}(R_{c_{if}})\right|} , \tag{5a}$$

$$B(\lambda) = \frac{4\pi^2 \mathrm{e}^2 \hbar}{mc} \frac{R_{AX}^2 f(R_{AX})}{\left|\Delta'_{AX}(R_{AX})\right|} , \tag{5b}$$

$$C(\lambda) = -\frac{V_i(R_{AX}(\lambda)) - V_i(\infty)}{k} . \tag{5c}$$

The first term in (4) corresponds to contributions to the total absorption coefficient coming from the transitions at long-range internuclear distances, which include all electronically allowed transitions from ground states to upper states of gerade and ungerade symmetry. R_{cif} denotes the outermost Condon points for each transition located at large internuclear distances, and the summation goes over all transitions, which have contribution in the same wavelength region. This term is temperature independent (dotted line in Fig. 3).

The second term in (4) corresponds to the contributions to the total absorption coefficient coming from the $1(X)\ ^1\Sigma_g^+ \rightarrow 1(A)\ ^1\Sigma_u^+$ transitions with Condon point R_{AX} in the internuclear range 6.9–7.7 Bohr. This term is temperature dependent (dashed line in Fig. 3).

Functions $A(\lambda)$, $B(\lambda)$, and $C(\lambda)$ ((5a)–(5c)) can be represented in an approximate form by a simple analytical formula, valid in the temperature range 500–700 K. The relevant expressions are given in Appendix A, and with use of (4), represent a simple numerical fit of the calculated theoretical absorption coefficient. The analytical formula obtained reproduces the calculated absorption coefficient within an accuracy of 5%. This approximate form can be used in practice for the determination of the atom number density and temperature of rubidium vapor.

4 Results and discussion

The existence of the two contributions to the total absorption coefficient in (4) is the basis of our method for the simultaneous determination of the temperature and concentration. As can be seen from Fig. 3, the general shape of the absorption line wings is mostly determined by the temperature-independent part alone. The temperature-dependent part contributes only as a continuous background with a temperature-dependent slope.

Knowing this, we can guess a value for the square of the concentration, $\tilde{N}^2$, multiply it by the temperature-independent part of the reduced absorption coefficient, $A(\lambda)$, from our simulation, and then subtract this quantity from the measured absorption coefficient $k_{\exp}(\lambda)$. Assuming that the measured absorption coefficient, at a given temperature T and concentration N, can be described by (4), the subtraction gives

$$k_{\exp}(\lambda) - \tilde{N}^2 A(\lambda) = (N^2 - \tilde{N}^2)A(\lambda) + N^2 B(\lambda) \times \exp\left(C(\lambda)/T\right) . \tag{6}$$

If our initial guess $\tilde{N}$ is close to the true concentration $N(\tilde{N} \approx N)$, the result of the subtraction should have the

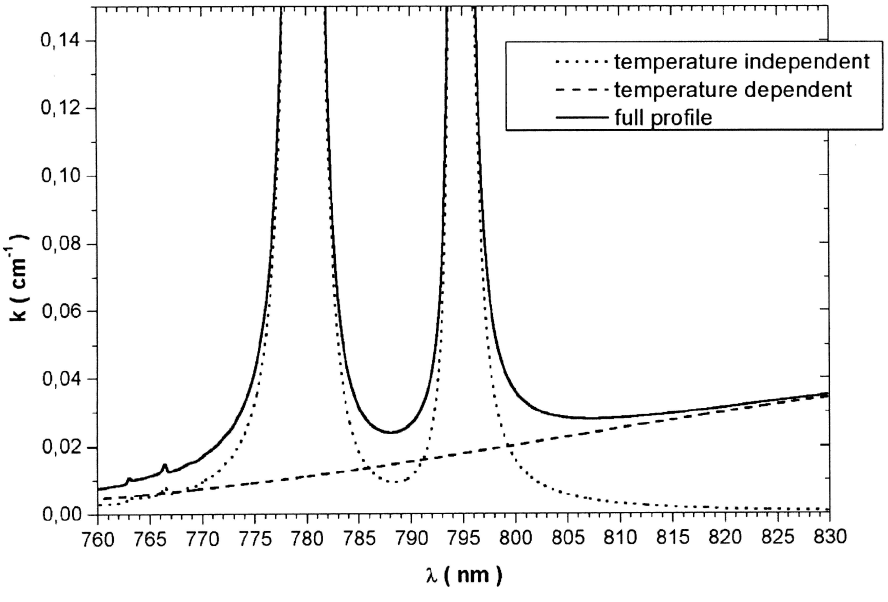

FIGURE 3 Total absorption coefficient calculated in the wings of the Rb resonance lines (*solid line*). Temperature-independent (*dotted line*) and temperature-dependent (*dashed line*) contributions to the absorption coefficient

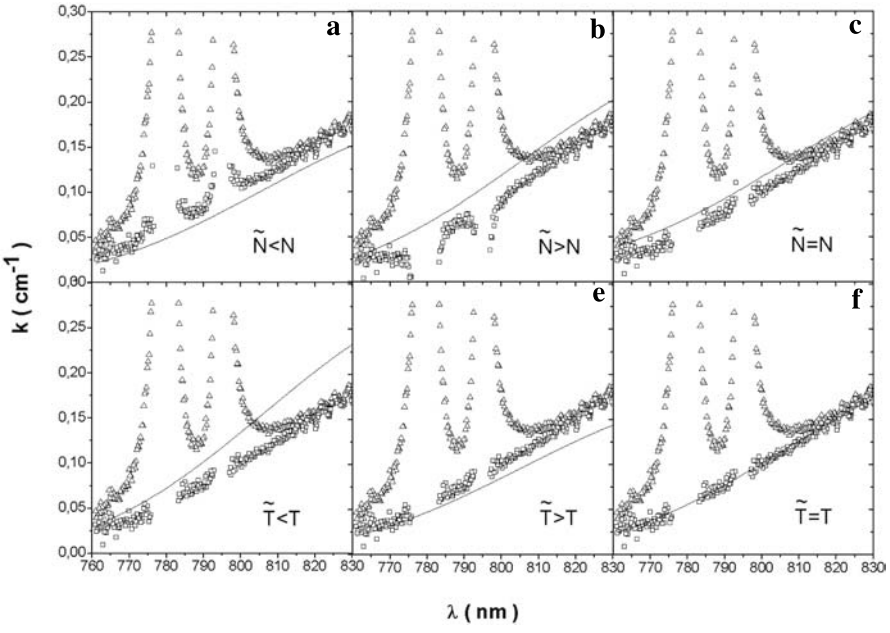

FIGURE 4 Illustration of the procedure used for the simultaneous determination of the concentration and temperature of the rubidium vapor. *Triangles*, measured absorption coefficient; *squares*, calculated temperature-independent absorption profiles subtracted from the corresponding measured profiles. $\tilde{N}$, guessed value of the concentration; N, true concentration; $\tilde{T}$, guessed temperature; T, true temperature

shape of the temperature-dependent part:

$$k_{\exp}(\lambda) - \tilde{N}^2 A(\lambda) = \tilde{N}^2 B(\lambda) \exp\left(C(\lambda)/T\right). \tag{7}$$

Now we can simulate the temperature-dependent part to match the left side of (7) and thus determine the temperature.

In practice, the method is carried out in several iterative steps, as shown in Fig. 4. The first step is to guess the initial value of the concentration and calculate the temperature-independent part of the absorption coefficient. Following (6), the calculated profile is then subtracted from the measured absorption coefficient (the curve represented with squares in Fig. 4). The result of the subtraction shows disagreement with the shape of the calculated temperature-dependent part if the guessed concentration is different from the true concentration (Fig. 4a and b). This disagreement is particularly evident in the near-wings of the Rb resonance lines. In order to describe the shape of the temperature-dependent part, a guessed value of the temperature is used. Through an iterative procedure, the subtraction profile can be adjusted to reproduce the shape of the temperature-dependent part of the absorption coefficient (Fig. 4c). In this way, the concentration is determined and its value is used to determine the temperature by means of (7). In Fig. 4c we can see the disagreement of the theoretical temperature-dependent part and the corresponding subtraction profile. This is a result of the constant background in the measured absorption coefficient, which was explained previously in detail (see (2)). Furthermore, this constant background is deducted from the subtraction profile. Different temperatures result in different slopes of the temperature-dependent curves (Fig. 4d and e). Through an iterative procedure, the temperature is varied until the best agreement between the calculated temperature-dependent part and the subtracted profile is obtained (Fig. 4f). The spectral region ($\Delta\lambda = \pm 2$ nm) around the centers of the resonance lines is not included in these considerations because of the optically thick vapor $kL \gg 1$. Figure 4 shows a quantitative description of the (N, T) determination. With the (N, T) pair approximately determined following the steps shown in Fig. 4, we enter into the least-squares two-parameter fitting procedure. We change simultaneously, in arbitrary small steps, the (N, T) values until a minimum disagreement between the experimental and theoretical absorption coefficient profiles is obtained. The result of the least-squares two-parameter fitting procedure is a paraboloid-like surface and for $T = 605$ K and $N = 3.52 \times 10^{16}$ cm^{-3} is shown in Fig. 5.

The method presented was used for the determination of the rubidium vapor density and temperature in the temperature range 500–700 K, which approximately corresponds to an optical thickness range of $0.12 \leq kL \leq 0.3$. For vapor temperatures below 500 K ($N_{\mathrm{Rb}} = 0.21 \times 10^{16}$ cm^{-3}), the temperature-dependent part of the absorption coefficient is negligible. Likewise, because of the optically thin vapor, the applied method has to be modified to take into account the transitions to upper states located at the energies approximately equal to the energies of the atomic resonances. This,

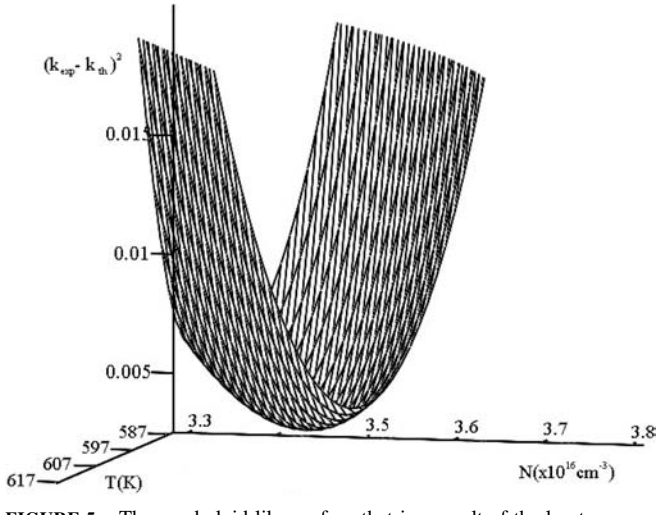

FIGURE 5 The paraboloid-like surface that is a result of the least-squares two-parameter fitting procedure for $T = 605$ K and $N = 3.52 \times 10^{16}$ cm^{-3}

however, exceeds the domain of applicability of the semiclassical quasi-static approximation that was used. For the temperatures above 700 K, due to the optically thick vapor, it was not possible to gain any useful information concerning the wings of the resonance lines. By changing the vapor column length L it could be possible to extend the domain of applicability of this method for temperature and concentration determination far beyond that considered in this work. For example, extra thin cells could be used [25, 26] for the determination of higher vapor temperatures and densities.

4.1 *Nearly homogeneous rubidium vapor*

The absorption coefficient of the rubidium vapor generated in the sapphire cell in the wavelength range 760–830 nm at various vapor temperatures is shown in Fig. 6. For each measured absorption coefficient the corresponding calculated one is presented, showing the excellent agreement between the measurement and calculation. The measured absorption coefficient profiles that are presented were corrected for the constant background. The spectral feature appearing around 765 nm is connected with the Rb_2 $1(a)\ ^3\Sigma_u^+$ $(1_u) \rightarrow 1\ ^3\Pi_g$ (0_g^+) transition, one of the well-known rubidium triplet satellite bands [19]. At temperatures above 550 K, at wavelengths above 810 nm the undulations from bound–bound Rb_2 X–A transitions are readily observable. Our semiclassical calculations represent averaged quantum mechanical calculations, as was shown in [27, 28].

The values of the atom number density and temperature that were obtained using the developed method are shown in Fig. 7. The level of vapor homogeneity was determined by the measured temperature difference between side parts and the central part of the cell (T_1–T_o, shown in Fig. 7). The temperatures that were determined fell in this measured temperature range, with a tendency be close to the side part (higher) temperatures (T_1). This behavior is expected and is a result of the experimental design of the oven, which provides a much longer higher temperature (T_1) vapor length than the

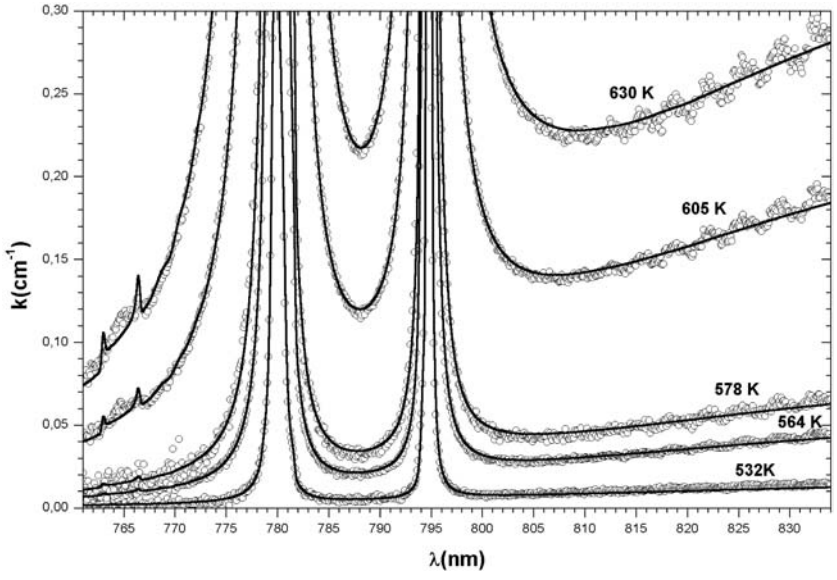

FIGURE 6 Measured (*circles*) and calculated (*solid line*) absorption coefficients of a nearly homogeneous rubidium vapor generated in the sapphire cell in the wavelength range 761–834 nm at various vapor temperatures. The given temperatures were obtained by using the procedure described in Fig. 4

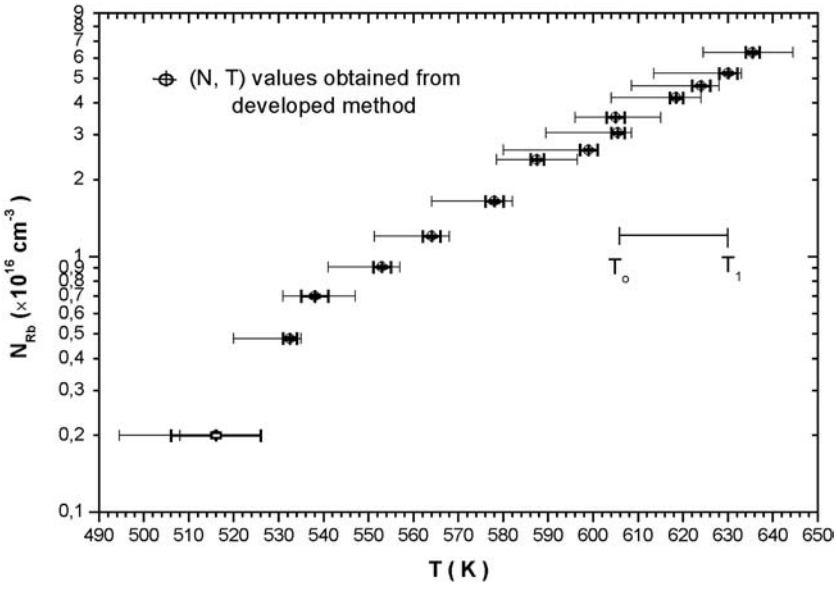

FIGURE 7 Atom number density and temperature determined in a nearly homogeneous rubidium vapor, obtained using the method developed (*circles with error bars*). T_1, *side part* (higher) temperatures; T_o, *central part* (lower) temperatures

lower temperature (T_o) vapor column length. The equilibrium temperatures corresponding to the concentrations determined from the presented method fell very close to the temperature of the central (lower) part of the cell. Therefore, in the experimental arrangement used, the effective atom concentration was mostly determined by the temperature of the central part (T_o), whereas the temperature of the side parts (T_l) determined the effective vapor temperature.

The least-squares fitting procedure was used to evaluate the uncertainties of the concentrations and temperatures determined by the applied method. The precision of the atom concentration determination for the applied method was better than 2.5%. The precision of the temperature determination was better than ± 3 K. As can be seen from Fig. 6, the uncertainty at the lowest temperature was large. However, the accuracy of our method depends on the accuracy of the calculated potential curves and transition dipole moment functions, which certainly had larger error bars than the quoted error bars in the precision assessment. We expect that the density determination is more accurate than the temperature determination. This is because the first relies on more accurate long-range potential curves and the relevant transition dipole moment functions, whereas the latter depends on the short-range behavior of the A–X difference potential and the corresponding dipole moment function.

4.2 *Inhomogeneous rubidium vapor*

For the generation of the inhomogeneous vapor in the sapphire cell, the third middle heater was applied (see Sect. 2). The effective Rb atom concentrations and temperatures that were determined for the inhomogeneous vapor, for various temperature differences between the side and central parts of the cell, are presented in Table 1.

In order to illustrate the physical conditions of the vapor inside the sapphire cell a simple heat diffusion model is employed. The temperature distribution inside the sapphire cell is a function of the boundary conditions, which are given by the measured outer temperatures of the central part (T_o) and the side parts of the cell (T_l). To evaluate the temperature distribution inside the cell, the heat diffusion equation given by (8) needs to be solved:

$$\nabla^2 T = \frac{1}{\kappa}\frac{\partial T}{\partial t}\,, \tag{8}$$

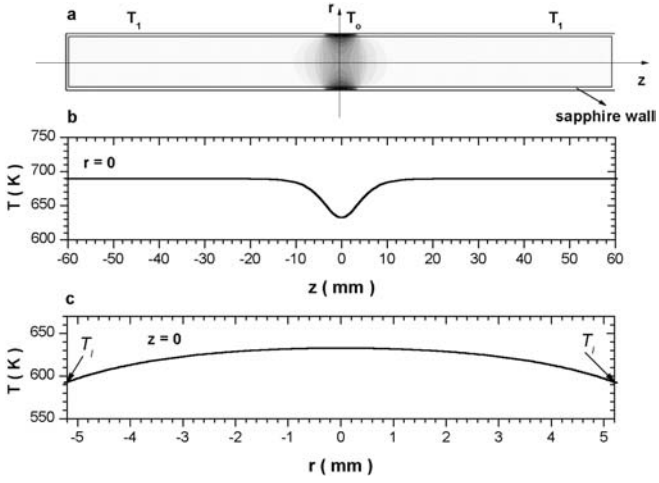

FIGURE 8 The temperature distribution inside the sapphire cell obtained from the simple diffusion model: **a** the temperature distribution across the plane passing through the center of the cell, for the case of an inhomogeneous rubidium vapor ($T_o = 550$ K, $T_l = 689$ K), and the temperature distribution along the longitudinal (**b**) and radial (**c**) axes of the cell

where T is the temperature, κ thermal diffusivity, and t is the time. Under steady state conditions (8) simplifies to

$$\nabla^2 T = 0\,. \tag{9}$$

The relation (9) is solved numerically by writing the Laplacian operator in cylindrical coordinates. The temperature distribution across the plane passing through the center of the cell for $T_o = 550$ K and $T_l = 689$ K is shown in Fig. 8a. The density of the dots is inversely proportional to the temperature (higher density – lower temperature). Figure 8b and c show the temperature distribution along the longitudinal ($r = 0$) and radial ($z = 0$) axes of the cell, respectively.

Knowing the temperature distribution across the volume of the cell, the distribution of the atoms in the cell (concentration) can be calculated following the equation of state for a perfect gas [15]:

$$N(T) = \frac{p_l}{kT}\,, \tag{10}$$

where p_l is the rubidium vapor pressure inside the cell, determined by the lowest temperature point T_l of the vapor (the point of condensation) from the Nesmeyanov pressure curve, N is the concentration of the rubidium atoms, k is the Boltzmann constant, and T is the temperature. Due to

Experiment			This method		Diffusion model		
T_0 (K)	T_l (K)	ΔT(K)	T_{eff} (K)	N_{eff} ($\times 10^{16}$ cm^{-3})	T_l (K)	T_{eff} (K)	N_{eff} ($\times 10^{16}$ cm^{-3})
537	568	31	573 ± 3	0.89 ± 0.01	546.6	566.9 ± 0.3	0.91 ± 0.06
513	546	33	575 ± 7	0.46 ± 0.01	523.2	544.8 ± 0.3	0.45 ± 0.04
543	580	37	584 ± 3	1.11 ± 0.01	554.4	578.6 ± 0.4	1.13 ± 0.09
604	672	68	677 ± 5	5.50 ± 0.10	625.0	669.5 ± 0.6	6.28 ± 0.68
543	614	71	606 ± 3	1.58 ± 0.01	565.0	611.4 ± 0.6	1.45 ± 0.20
541	642	101	637 ± 5	2.10 ± 0.02	572.2	638.3 ± 0.9	1.71 ± 0.31
550	689	139	673 ± 5	3.70 ± 0.05	593.1	683.9 ± 1.3	2.80 ± 0.65

TABLE 1 The effective atom concentration and temperature determined by the method presented in this work, compared with the results obtained by the simple heat diffusion model

heat diffusion through the sapphire walls of the cell, the lowest vapor temperature T_1 is higher than the temperature T_0 measured at the outside walls of the central part of the cell (Fig. 7c).

The effective concentration and temperature of the rubidium atoms are then obtained by averaging the calculated concentration and temperature distributions across the whole volume of the cell. For the sake of comparison these effective values are also shown in Table 1. The uncertainties in the effective atom concentrations that were determined were rather large and increased with increasing $\Delta T(\Delta T = T_1 - T_o)$. This is a result of the approximate boundary conditions, which could not be appropriately measured (the temperature should be measured along the whole length of the cell with great spatial resolution, which exceeds the scope of this work).

5 Conclusion

The theoretical absorption profiles show good agreement with experimental profiles. This provides a good foundation for developing a method for atom number density determination. The analysis of all the transitions that contribute to the absorption coefficient shows that in addition to the atom number density, in the temperature range 500–700 K, the temperature of the Rb vapor can also be independently determined.

The method was tested on a sapphire cell system, first under nearly homogeneous vapor conditions and then with deliberately imposed inhomogeneous temperature and density distributions. The characterization of such a system by a simple steady-state heat diffusion model shows reasonable agreement with our method. The statistical error of the method was better than 2.5% for concentration determination and ±3 K for temperature determination (in the temperature range considered).

An obvious advantage of this method is its widespread applicability in all cases in which absorption measurements of resonances lines can be easily performed. However, the method is applicable only if theoretical profiles are available, and this should be the case for all pure alkali vapors. The simultaneous determination of atom number density and temperature can be carried out in the case of rubidium vapor in thermal equilibrium. The method comprises experiments with various cells and heat-pipe ovens. Initially, our motivation for the development of such a method was to characterize the rubidium vapor generated in a home-made crossed heat-pipe oven used in our laboratory for various laser spectroscopy measurements. In situ temperature measurements of Rb vapor generated in such an oven are difficult due to practical reasons. Using the present method we determined the atom number concentration and temperature of rubidium vapor generated under different conditions of operation of the heat-pipe oven.

The cases of a superheated vapor (see e.g. [29]) or different types of discharge plasmas with rubidium vapor may be of interest for future investigation. Laser-produced neutral clouds and plasmas with alkalis could also be interesting to study in the near future [30, 31]. In general, the wings of resonance lines of alkali atoms offer new possibilities in neutral vapor and plasma diagnostics, which is a natural extension of the early predictions made by Movre and Pichler [32].

Modification of this method could, in addition to resonance broadening, include the effect of foreign-gas broadening. In that way it would be possible to apply this method to the investigation and characterization of the atmospheres of brown dwarfs and other more complex systems in which pressure broadening by H_2 and He is the dominant broadening mechanism [33].

ACKNOWLEDGEMENTS We acknowledge support from the Ministry of Science and Technology of the Republic of Croatia, the European Community Research Training Network, FW 5, the Alexander von Humboldt Foundation, and COST 529: "New Light Sources for the 21st century". Fruitful discussions with D. Sarkisyan, S. Milošević, D. Veža, and M. Movre are gratefully acknowledged.

Appendix

Approximate forms of the functions $A(\lambda)$, $B(\lambda)$, and $C(\lambda)$ valid in the temperature range 500–700 K are:

$$A(\lambda) = \left\{ \Theta(\lambda_1 - \lambda) \left[\frac{2039}{(\lambda_1 - \lambda)^2} + \frac{746}{(\lambda_1 - \lambda)^{1.68}} \right] + \Theta(\lambda - \lambda_1)\Theta(\lambda_2 - \lambda) \left[\frac{2166}{(\lambda - \lambda_1)^2} - \frac{137}{(\lambda - \lambda_1)^{1.13}} \right] + \Theta(\lambda_2 - \lambda) \left[\frac{706}{(\lambda_2 - \lambda)^2} + (\lambda_2 - \lambda)^{0.011} \right] + \Theta(\lambda - \lambda_2) \left[\frac{899}{(\lambda - \lambda_2)^2} + \frac{222}{(\lambda - \lambda_2)^{1.224}} \right] \right\} \times 10^{-36} \ [\mathrm{cm}^5] \ , \quad \text{(A.1)}$$

$$B(\lambda) = \left[9.62753 \times 10^{-3} + 2.28637 \times 10^{-5} (\lambda - \lambda_2) \right] \times 10^{-36} \ [\mathrm{cm}^5] \ , \quad \text{(A.2)}$$

$$C(\lambda) = 5392.7053 + 15.664(\lambda - \lambda_2) - 0.15992(\lambda - \lambda_2)^2 \ [\mathrm{K}] \ . \quad \text{(A.3)}$$

λ_1 and λ_2 are the wavelengths of the Rb $D2$ and $D1$ resonance line centers, respectively. $\Theta(\lambda)$ is the Heaviside step function, N is the concentration of Rb atoms, and T is their temperature. The wavelengths in (A.1)–(A.3) should be given in nanometers.

We have described the temperature-independent $A(\lambda)$ function in (5a) as comprising four contributions, which represent the blue and red wings of the $D2$ and $D1$ resonance lines. The leading term in each bracket is approximated by the usual form characteristic for the resonance broadening $1/(\lambda - \lambda_a)^2$. The second term in each bracket has no obvious physical meaning, but is used here as the best fit that "takes into account" other interaction constants and variable oscillator strengths. $B(\lambda)$ and $C(\lambda)$ from relations (5b) and (5c) are slowly varying functions of λ, and the linear and quadratic approximations, respectively, appear to be sufficiently accurate for the reliable application of the method presented in this paper.

REFERENCES

1 W. Demtröder: *Laser Spectroscopy: Basics Concepts and Instrumentation* (Springer, New York 2002)
2 P.W. Wang, A. Gallagher, J. Cooper: Phys. Rev. A **56**, 1598 (1997)
3 A.N. Nesmeyanov: *Vapor Pressures of Chemical Elements* (Elsevier, New York 1963)
4 A. Gallagher, E.L. Lewis: J. Opt. Soc. Am. **63**, 864 (1973)
5 A.C.G. Mitchell, M.W. Zemansky: *Resonance Radiation and Excited Atoms* (Cambridge University Press, Cambridge 1961)
6 A. Thorne, U. Litzén, S. Johansson: *Spectrophysics* (Springer, Berlin 1999)
7 K. Niemax, G. Pichler: J. Phys. B: At. Mol. Phys. **8**, 179 (1975)
8 M. Movre, R. Beuc: Phys. Rev. A **31**, 2957 (1985)
9 R. Beuc, M. Movre, Č. Vadla: J. Phys. B: At. Mol. Phys. **15**, 1333 (1982)
10 V. Horvatić, M. Movre, R. Beuc, Č. Vadla: J. Phys. B: At. Mol. Opt. Phys. **26**, 3679 (1993)
11 D.H. Sarkisyan, A.S. Sarkisyan, A.K. Yalanusyan: Appl. Phys. B **66**, 241 (1998)
12 T. Ban, H. Skenderović, R. Beuc, G. Pichler: Europhys. Lett. **48**, 378 (1999)
13 H. Skenderović, R. Beuc, T. Ban, G. Pichler: Eur. Phys. J. D **19**, 49 (2002)
14 D. Sarkisyan: private communication
15 P.W. Atkins: *Physical Chemistry* 6th edn. (Oxford University Press, New York 2000)
16 M. Foucrault, P. Millie, J.P. Daudey: J. Chem. Phys. **96**, 1257 (1992)
17 M. Marinescu, A. Dalgarno: Phys. Rev. A **52**, 311 (1995)
18 J.S. Cohen, B. Schneider: J. Chem. Phys. **61**, 3240 (1974)
19 M.-L. Almazor, O. Dulieu, F. Masnou-Seeuws, R. Beuc, G. Pichler: Eur. Phys. J. D **15**, 355 (2001)
20 R. Beuc, H. Skenderović, T. Ban, D. Veža, G. Pichler, W. Meyer: Eur. Phys. J. D **15**, 209 (2001)
21 M. Movre, G. Pichler: J. Phys. B: At. Mol. Phys. **10**, 2631 (1977)
22 J. Szudy, W.E. Baylis: J. Quant. Spectrosc. Transfer **15**, 641 (1975)
23 J. Tellinghuisen, G. Pichler, G.W. Snow, M.E. Hillard, R.J. Exton: Chem. Phys. **50**, 313 (1980)
24 V. Kokoouline, O. Dulieu, F. Masnou-Seeuws: Phys. Rev. A **62**, 022 504 (2000)
25 M. Otake, K. Fukuda, M. Tachikawa: Appl. Phys. B **74**, 503 (2002)
26 D. Sarkisyan, D. Bloch, A. Papoyan, M. Ducloy: Opt. Commun. **200**, 201 (2001)
27 H.-K. Chung, K. Kirby, J.F. Babb: Phys. Rev. A **63**, 032 516 (2001)
28 L.K. Lam, A. Gallagher, M.M. Hessel: J. Chem. Phys. **66**, 3550 (1977)
29 T. Ban, H. Skenderović, S. Ter-Avetisyan, G. Pichler: Appl. Phys. B **72**, 337 (2001)
30 A.G. Leonov, A.A. Rudenko, A.N. Starostin, M.D. Taran, D.I. Chekhov, I.I. Ykunin: J. Exp. Theor. Phys. **95**, 242 (2002)
31 F.T. Ferguson, J.A. Nuth III: J. Chem. Phys **113**, 4093 (2000)
32 M. Movre, G. Pichler: J. Phys. B: At. Mol. Phys. **13**, 697 (1980)
33 A. Burrows, W.B. Hubbard, J.I. Lunine, J. Liebert: Rev. Mod. Phys. **73**, 719 (2001)